



The effect of interstitial fluid on the machining behaviour of cortical bone

Jose A. Robles-Linares, Zhirong Liao^{*}, Dragos Axinte, Andres Gameros

Machining and Condition Monitoring Group, Faculty of Engineering, University of Nottingham, Nottingham NG7 2RD, UK

ARTICLE INFO

Associate Editor: Erhan Budak

Keywords:

Bone cutting
Interstitial fluid
Chip formation
Surface damage
Necrosis
Internal irrigation

ABSTRACT

Bone machining research is usually conducted ex-vivo with standard laboratory equipment, implying mostly that the cutting process takes place in dry state. While these studies are useful for understanding the bone cutting process, they cannot represent the real clinical cutting condition due to the disregard of internal irrigation (i.e., interstitial fluid and blood within the tissue's vascular porosities). As bone possesses ca. 20 % water, internal irrigation can influence the bone's properties (e.g., shear strength, friction coefficient) and alter the cutting mechanism and surface deformation (e.g., crack formation, smearing). Hence, to study the ex-vivo bone cutting process in an internally irrigated state, a novel machining and pumping setup is proposed here, which enables a scenario closer to a surgical condition than the traditional dry machining method. Cutting tests demonstrated that portions of bone near the fluid-filled porosities possess shear strength and friction coefficient gradients due to the bone's permeability. This resulted in machining forces and necrosis up to 52 % and 55 % lower than in dry bone, respectively. A cutting forces model was developed considering the internal irrigation condition and the randomness and anisotropy of the tissue. Moreover, it was found that internal irrigation can change the chip formation mechanism and induce minimised surface morphological damage due to the minimised friction between the tool and the cutting surface in near-porosity sites. This research highlights the importance of conducting bone machining research with the consideration of internal irrigation, an imperative aspect to more realistically mimic surgical scenarios in a laboratory environment.

1. Introduction

Bone cutting is a common process in orthopaedics, dentistry and neurosurgery that comprises both simple interventions (e.g., hole drilling) and complex procedures (e.g., joint replacement involving machined surface matching implant surface). However, bone cutting is challenging both in terms of machining analysis (Liao and Axinte, 2016) and damage assessment (Robles-Linares et al., 2021) due to its intricate hierarchical composite-like microstructure (Tan et al., 2021). Engineeringly, cortical bone consists of an arrangement of osteons (i.e., the fibres, running through the principal loading direction in the bone) (Heřt et al., 1994) within an interstitial lamellae (i.e., the matrix) composed of old osteons that have been partially resorbed during the remodelling process of the bone (Currey, 2002). Further, its porous structure contains the blood, nerve and interstitial fluid supplies (Cowan and Cardoso, 2015) that are necessary for the living tissue. As consequence, machining-induced strains and temperatures in cortical bone are difficult to analyse; therefore, vast amount of research has focused on improving the understanding of bone as a material that is subjected to

mechanical loads, such as under machining conditions.

Orthogonal cutting of bone has been extensively studied with the principal aim of understanding its cutting mechanisms under different machining conditions. Even the earliest reports on the cutting mechanisms of cortical bone (Jacobs et al., 1974; Wiggins and Malkin, 1978) showed a dependency of the chip morphology on both the cutting direction (i.e., relative to the principal osteon direction) and the depth of cut (DOC), where a small DOC was associated with continuous chips and a smooth surface, and a large DOC with a fractured or segmented chip and a rough surface. Additionally, the interface between the osteons and the interstitial lamellae (i.e., the cement line) was associated with crack propagation due to its lower strength when compared to both the osteons and the interstitial lamellae (Krause, 1987). More recent studies have confirmed that continuous or semi-continuous chips occur with a DOC lower than 80 μm at low (12.5 $\mu\text{m/s}$) (Sugita and Mitsuishi, 2009), intermediate (8 m/s) (Feldmann et al., 2017) and high (>15 m/s) (Sugita et al., 2014) cutting speeds, thus highlighting that bone's anisotropy and DOC are far more relevant in the cutting mechanism than the strain rate itself.

^{*} Corresponding author.

E-mail address: zhirong.liao@nottingham.ac.uk (Z. Liao).

<https://doi.org/10.1016/j.jmatprotec.2022.117697>

Received 22 April 2022; Received in revised form 6 June 2022; Accepted 20 June 2022

Available online 22 June 2022

0924-0136/© 2022 The Author(s). Published by Elsevier B.V. This is an open access article under the CC BY license (<http://creativecommons.org/licenses/by/4.0/>).

Contrary to the machining of soft tissues, which exhibit a large viscoelastic behaviour (Chen et al., 2021), bone possesses a ductile-to-brittle performance. Three main cutting modes can be identified in bone machining, and these depend on both the cutting direction and, mainly, the DOC. The modes show a transition of a ductile behaviour at low DOC to a brittle behaviour at large DOC. When the DOC is small (usually less than 13 μm), the cutting energy promotes plastic deformation, but not cracking (Feldmann et al., 2017), thereby producing a continuous chip (i.e., ductile behaviour) that is in compliance with the Erns-Merchant principle (Shaw, 2005); this cutting mode is known as shear cutting (SC) mode. Further, when the DOC is at intermediate values (usually between 13 and 70 μm), the chip volume is larger and it hinders plasticity, while enabling cracking to occur along the shear plane, thereby producing a series of discrete segments of chip (Liao and Axinte, 2016); this cutting mode is referred to as shear-crack cutting (SCC) mode and is characterised by its semi-brittle nature. Finally, when the DOC is large (>70 μm), the cutting and thrust forces play a more important role since their combined actions is enough to surpass the fracture toughness of the bone, thereby enabling a fracture cutting (FC) mode (i.e., brittle behaviour) in the chip formation mechanism (Liao and Axinte, 2016). Naturally, these cutting modes have a direct effect on the machined surface quality, where a SC mode can be associated with smooth surfaces, while the FC mode with rougher surfaces (Bai et al., 2020). As such, researchers are exploring ways of increasing the material removal rate without directly increasing the DOC, such as with ultrasonic vibration assisted machining (Yang et al., 2020) and improved tool design (Shu et al., 2020).

Due to the complexity of the bone cutting process, modelling it is a challenging task. As such, a significant number of papers have been reported, principally employing Finite Element Method (FEM) for the prediction of temperatures, cutting forces and chip formation (Marco et al., 2015). This has been usually done by adapting isotropic metal cutting models (e.g., Johnson-Cook model) (Baro and Deoghare, 2018; Childs and Arola, 2011), considering anisotropy by assigning different properties to each microconstituent of the bone (Hage and Hamade, 2013; Shu and Sugita, 2020) or by simply designating distinct properties depending on the cutting direction at the macroscale (Santiuste et al., 2014).

Empirical models have also been proposed for describing the orthogonal cutting process. For instance, it has been shown that the friction coefficient (μ), necessary for predicting the cutting and thrust forces, could be modelled as a function of DOC, in the form $\mu = \mu_0 h^c$, where μ_0 and h are the experimental calibration constants (Liao et al., 2019). Cutting temperature predictions during machining could also be performed empirically, based on the density distribution of the bone by assuming that a denser region produces a larger cutting force value, thereby increasing heat generation (Feldmann et al., 2016); however, this requires experimental constants and local density measurements, also accompanied by FEM.

Due to the semi-brittle nature of cortical bone, a fracture mechanics based cutting model has been proposed to explain the chip formation and cutting process in orthogonal cutting, by allowing the calculation of the mean cutting and thrust forces mechanistically (Liao and Axinte, 2016); thereby also providing the threshold DOC between each cutting mode (SC, SCC, FC). This mechanistic model only requires the mean values of the mechanical properties of the bone in the different cutting directions and for each cutting mode.

Similar to metal cutting, where the surface integrity post-machining is greatly relevant to the functional performance of structural components (la Monaca et al., 2021; Liao et al., 2021), bone machining can be easily damaged during a material removal process and impact the tissue's behaviour post-surgery (Karaca et al., 2011). Thus, additionally to understanding the cutting mechanism in cortical bone, there is also the imperative need to assess bone damage post-machining because, being a living tissue, not only is the mechanical integrity of relevance, but the wellbeing of the cells (i.e., osteocytes) is of utmost importance. For the

cells to perform their vital functions, they must remain below a certain temperature-time threshold (Hancox, 1972); usually defined as 47 °C for 1 min (Augustin et al., 2008) or 55 °C for 30 s (Hillery and Shuaib, 1999), which can be easily surpassed during a machining process. When the temperature surpasses this threshold, it generates cellular death (i.e., necrosis), which compromises the metabolism and remodelling process of the bone. Machining-induced necrosis can be directly assessed with histology; this has been demonstrated for both conventional (Robles-Linares et al., 2021) and non-conventional (Robles-Linares et al., 2022) machining by directly measuring the necrotic depth in the machined bone subsurface, which is enabled due to the clear distinction between 'death' and 'alive' osteocytes that histological methods generate (Hancox, 1972). To minimise necrosis, external cooling (i.e., saline solution) is usually employed with the intention of minimising the cutting temperatures. However, even with this traditional cooling method, the coolant cannot penetrate into the highest temperature zone (i.e., the tool-chip interface), similarly as reported in metal cutting with conventional cutting fluids (Sugihara et al., 2021).

While all the above cutting mechanisms and cutting models are valuable for understanding bone under machining conditions, they have typically neglected the in-vivo conditions bone, as they have been conducted in dry cutting conditions and considering bone as a block of solid material. However, bone is a porous structure that contains fluid flow within; in fact, intraosseous blood flow and interstitial fluid can help to dissipate the heat generated during the bone cutting process (Hillery and Shuaib, 1999), and consequently this should have a direct effect on the necrotic damage that is assessed with histology. Additionally, bone has a very low thermal conductivity (Feldmann et al., 2018), but it has been shown that blood flow and interstitial fluid significantly increases the effective thermal conductivity of the tissue (Li et al., 2014), which implies that necrosis should be hindered due to the fluid presence in the internal porosities of the bone. It is believed that this internal irrigation condition can also affect other properties that impact the cutting process (e.g., friction coefficient, shear strength). Nevertheless, no studies have shown the effect of blood and interstitial fluid on machining of cortical bone.

While dry bone cutting studies are useful, realistic and necessary for understanding the bone cutting mechanisms (i.e., cutting forces, chip formation), they are not comprehensive due to their lack of consideration of internal irrigation (i.e., presence of fluid flow in the vascular porosities of the bone), as the fluid presence in the porosities will locally affect the lubrication in the bone-tool interface. Moreover, while external flood cooling has typically been employed as a precautionary measure for avoiding necrosis, it does not allow for understanding the effect of internal irrigation in terms of neither temperature distribution nor necrotic damage, as the fluid presence in the porosities will not only affect the lubrication, but also the cooling mechanism in the cutting zone.

To investigate the role of internal irrigation (i.e., cooling, lubricating) on the cutting mechanism and necrotic damage of cortical bone, this paper presents a novel laboratory setup that allows for mimicking in-vivo conditions (i.e., internally irrigated bone) by pumping a fluid through the natural vascular porosities of the bone, so that the real (i.e., closer to a surgical environment) cutting conditions can be replicated. Additionally, a mechanistic model was developed to consider the local variations of friction and shear strength due to the fluid supply via internal irrigation and a series of tests have been performed to show the relevance of internal irrigation in the cutting mechanism and necrosis of cortical bone. As such, this paper emphasises, for the first time, that internal irrigation (i.e., which mimics in-vivo conditions) has a clear importance when studying the cutting mechanisms of bone and its response to cutting parameters.

2. The importance of internal irrigation and its influence on the bone cutting mechanism

Up to now there are no studies of the cutting mechanism of bone in-vivo. This is not surprising as, usually, the machinist requires additional equipment (e.g., high-speed cameras, thermocouples, load cells, etc). Indeed, there are studies on bone cutting done on experimental setups, but these are far from reality as the bone is a living structure where the blood and interstitial fluid are supplied via the vascular channels (i.e., Haversian and Volkmann's canals), and as mentioned above, there might be an influence of this local fluid (i.e., blood, interstitial fluid) supply upon the cutting mechanisms.

Here, a novel method is proposed to study the influence of local lubrication (see Fig. 1) that is provided by the blood and interstitial fluid supplied through the vascular porosities upon the cutting mechanism of the bone and its further influences on the level of damage on the living cells during cutting.

As such, Fig. 1 presents the real cutting conditions of living bone since the interstitial fluid presence in the natural porosities of the bone is considered. During the cutting process, the cutting edge will be in close contact with both bone material and porosities. However, due to the in-vivo conditions, the porosities are not empty, as they possess interstitial fluid inside (Cowin and Cardoso, 2015). This phenomenon enables a localised fluid effect on the cutting edge as it removes material: greater lubrication and cooling will take place in portions with fluid, whereas fluid-free portions will depict a dryer cutting behaviour (i.e., minimised cooling and larger friction).

As this might be an interesting and relevant problem in cutting bone structure, an original laboratory method to study this localised fluid effect during machining has been developed (see Fig. 2). This setup offers the possibility to study the specifics of cutting mechanisms of bone and make adaptations of the cutting models to reflect the influence of local lubrication provided by the pumped fluid through the bone sample, which ultimately mimics the interstitial fluid flow presence.

The setup consists of an additively manufactured assembly which serves to clamp a small bone sample over a dynamometer (Kistler type 9317 C) for a machining operation (see Fig. 2a), while also allowing for fluid pumping to take place, being the fixture the fluid inlet and the bone the fluid outlet (see Fig. 2b). This design offers the main advantage of permitting to pump fluid through the natural porosities of cortical bone (i.e., the Haversian and Volkmann's canals), thereby enabling a more realistic (i.e., closer to an in-vivo condition) laboratory setup for bone machining testing in a laboratory environment (see Fig. 2c). As an example, Fig. 2d depicts an orthogonal cutting section of cortical bone mounted on the setup and having saline solution pumped through its natural porosities.

This will be useful to understand the magnitude of living bone structure during and after cutting. During the cutting process, the

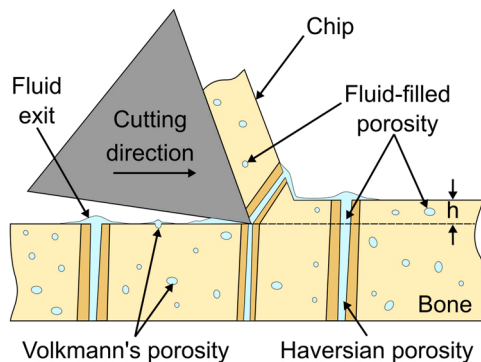


Fig. 1. Schematic representation of bone cutting in-vivo without external cooling, where the vascular porosities are filled with interstitial fluid, thereby acting as local lubrication points.

involved forces and chip formation mechanisms can be measured, recorded and analysed, which yields a more comprehensive machining understanding of this material. After cutting, the sample can be assessed with traditional engineering methods (e.g., SEM, surface roughness) and, additionally, the sample can be studied histologically to measure the necrotic extent induced by machining, thus enabling a damage evaluation that is highly relevant in the medical community. It is expected that all these measurable aspects depict a significant difference between dry bone (i.e., as traditionally tested in the scientific community) and irrigated bone (i.e., as enabled by the novel setup for mimicking in-vivo conditions).

2.1. Modelling of bone cutting considering the influence of local irrigation

Cortical bone machining research, usually conducted in dry, wet (external coolant delivery) or frozen states, have so far neglected the effect of interstitial fluid presence in the vascular porosity (VP) system (i.e., Haversian and Volkmann's canals) of the bone. Nevertheless, as explained previously this fluid presence is expected to alter the machining behaviour of cortical bone. Thus, to tackle this, local gradients of shear strength and friction coefficient near the VP pores have been considered to occur due to the permeability (Cowin and Cardoso, 2015) of bone near the VPs.

It is considered that the Haversian and Volkmann's porosities are filled with interstitial fluid and blood (see Fig. 3) and that due to the permeability of the bone, the fluid is radially absorbed into the cortical tissue, thereby increasing the lubrication near the canals and decreasing the shear strength of the bone in these zones. However, the effect is not the same throughout all this annular zone of lower properties. The region immediately surrounding the porosity will be highly permeable and therefore it is expected to have a lower friction coefficient (μ) and shear strength (τ) than regions away from the porosity in contact with the cutting edge. Therefore, an *affected zone* is introduced for both the friction coefficient and shear strength, where their values will be lower than in the bulk region away from the fluid.

To model the effects of interstitial fluid in the cutting process, it is necessary to consider variations in porosity and microstructural arrangements (i.e., interstitial lamellae, osteons and porosities exact locations) along the toolpath. To this end, an algorithm has been developed to have the capability of constructing a bone volume of specific dimensions, microstructural arrangements (including the VP) and randomness. This is based on a previous work (Robles-Linares et al., 2019), but some changes have been put in place to improve its usage in this specific application (i.e., bone cutting forces modelling).

In short, a set of inputs are fed to the algorithm, such as porosity range, cutting direction and osteon density. Using Boolean logic and vectorial algebra, the program yields a set of data that contains the location, direction and radius of each porosity in the bone workpiece. By defining a specific plane and cutting direction, the cutting surface is then obtained, yielding with exactitude the positions of the microstructures (i.e., interstitial lamellae, osteon, porosity) that will be in contact with the cutting edge along the toolpath; an example is shown in Fig. 4a for the case of transverse cutting direction. To this end, each porosity is regarded as an individual vector of specific length, direction and thickness (i.e., radius). Thus, by considering that the affected zone radius (r_{az}), as defined in Fig. 3, is a function of the porosity radius (r_{por}) then:

$$\gamma_{az} = \frac{r_{az} - r_{por}}{r_{por}} \quad (1)$$

where γ_{az} represents the ratio between the thickness of the affected zone and the porosity radius, which can be obtained experimentally.

Regarding the effect of the fluid within the affected zone radius, several aspects must be considered. First, the porosity volume (where $r < r_{por}$) is filled with fluid (i.e., not bone); as such, it can be regarded as

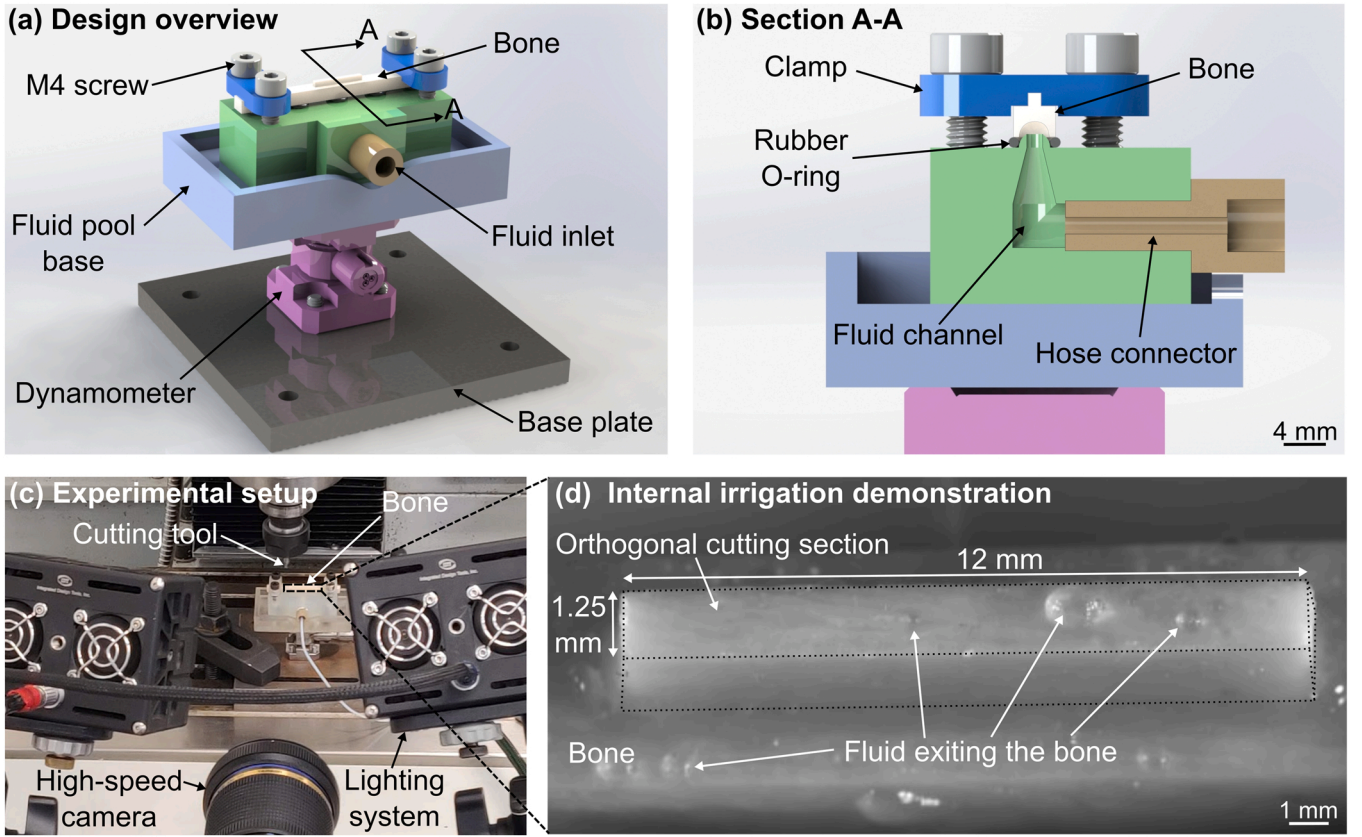


Fig. 2. Fixturing and pumping system for enabling the delivery of the interstitial fluid through the bone porosities during machining to mimic in-vivo conditions. (a) Design overview of the setup. (b) Cross section of the system, where the fluid channels that allow pumping fluid into the bone are visible. (c) Experimental setup. (d) Example of a bone sample with internal irrigation.

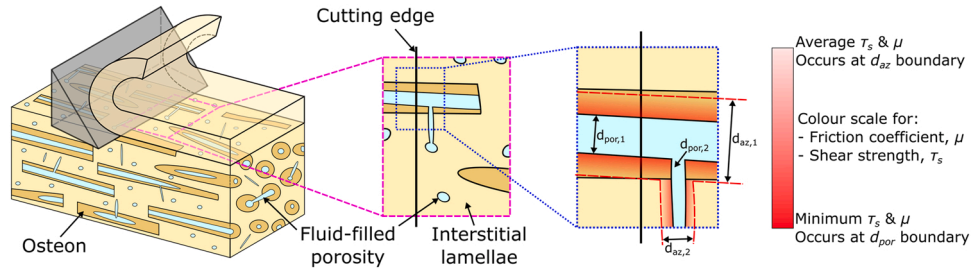


Fig. 3. Effect of interstitial fluid during bone machining. Near-porosity sites (i.e., affected zone) depict a linear gradient in shear strength and friction coefficient due to the permeability of the bone.

a void that does not contribute neither to shear strength nor to producing friction with the cutting edge, thus resulting in contributing with zero values to the cutting forces. Second, regions of the bone away from the affected zone (i.e., $r > r_{az}$) will behave as pristine bone, retaining unaffected properties. Third, the affected zone region ($r_{por} \leq r \leq r_{az}$) will depict a linear variation of its properties, where they will be at a minimum value larger than zero in the porosity wall ($r = r_{por}$) and a pristine value at the end of the affected zone ($r = r_{az}$). Thus, for the friction coefficient (μ):

$$\mu = \begin{cases} 0, & \forall r < r_{por} \\ \mu_0(1 - \beta_\mu) + (r - r_{por}) \frac{\mu_0 \beta_\mu}{r_{az,\mu} - r_{por}}, & \forall r_{por} \leq r \leq r_{az,\mu} \\ \mu_0, & \forall r > r_{az,\mu} \end{cases} \quad (2)$$

where β_μ represents the reduction ratio of the friction coefficient in the

porosity wall (r_{por}) when compared to the pristine value of the friction coefficient outside the affected zone (where $\mu = \mu_0$). Similarly, for the shear strength:

$$\tau = \begin{cases} 0, & \forall r < r_{por} \\ \tau_0(1 - \beta_\tau) + (r - r_{por}) \frac{\tau_0 \beta_\tau}{r_{az,\tau} - r_{por}}, & \forall r_{por} \leq r \leq r_{az,\tau} \\ \tau_0, & \forall r > r_{az,\tau} \end{cases} \quad (3)$$

where β_τ represents the reduction ratio of the shear strength in the porosity wall (r_{por}) when compared to the pristine value of the shear strength outside the affected zone (where $\tau = \tau_0$). Note how from Eq. (2) and Eq. (3), the affected zones and their respective reduction ratios are considered independently from each other when relating to either the friction coefficient ($r_{az,\mu}$ and β_μ) and the shear strength ($r_{az,\tau}$ and β_τ), respectively. This is conservatively considered this way, since it cannot

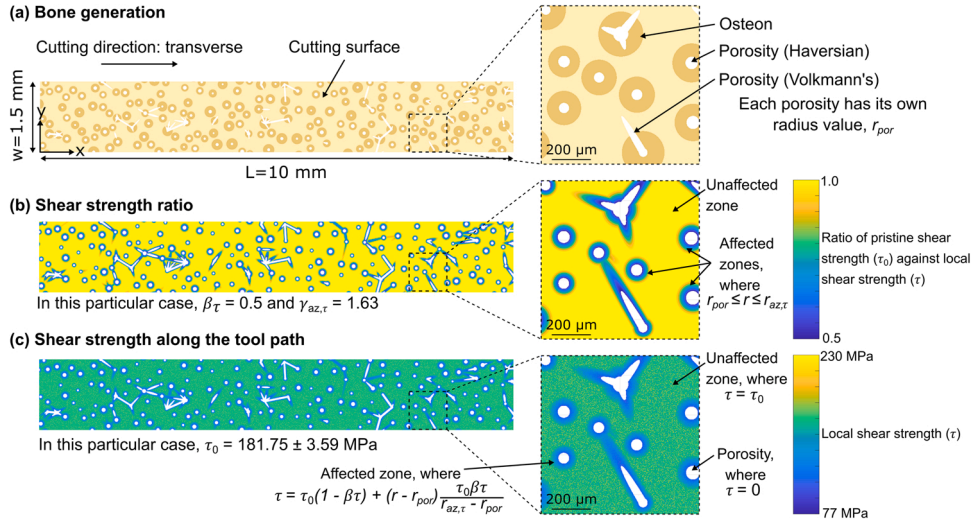


Fig. 4. Example of properties mapping (shear strength) along the toolpath for the case of transverse cutting direction. (a) Bone cutting surface generation. (b) Calculation of local property ratios with a linear gradient in the affected zones. (c) Calculation of the local value of properties.

be assumed that the fluid will affect two different properties in the same manner.

Therefore, in the bulk material (i.e., regions outside of the affected zone), the bone will possess its pristine properties of shear strength and friction coefficient, but as the cutting edge approaches the porosity, it will see a decrease in both shear strength and friction that goes from their average value (i.e., μ_0, τ_0) in the farthest region from the porosity ($r \geq r_{az}$), to a minimum value (i.e., defined by β_μ and β_τ) in the porosity wall ($r = r_{por}$). A set of machining trials conducted in bone samples with induced controlled porosities (i.e., micro-drilled holes) enabled the calculation of such experimental constants, which were found to be $\gamma_{az,\mu} = 2.18$ and $\beta_\mu = 0.08$ for the friction coefficient and $\gamma_{az,\tau} = 1.63$ and $\beta_\tau = 0.50$ for the shear strength. An example of this is shown in Fig. 4b and Fig. 4c for the case of shear strength along the toolpath when cutting in the transverse direction.

This part of the model could be regarded as the properties mapping stage (see stage 3 of Fig. 5), and it works in three main steps. First, a cutting surface is produced, where the microstructural arrangements along the toolpath are obtained via the bone generation algorithm (Fig. 4a). Second, the calculation of the ratio of shear strength and friction coefficient is done along the cutting surface, using the reduction ratios and affected zones (example shown in Fig. 4b). Third, once the ratio of each property is known along the surface, the local values are calculated for each node (Fig. 4c) by considering the mean value of the pristine property, its standard deviation and the local reduction ratio.

Once the properties mapping stage is finished, it allows to obtain the local values of shear strength and friction coefficient along the toolpath as function of position in the cutting surface, i.e., $\tau = \tau(x, y), \mu = \mu(x, y)$. Thus, this enables the calculation of the cutting forces along the toolpath. Employing the assumption of plane-strain conditions and that only shear and shear-crack cutting modes are present (i.e. plastic deformation dominates the process and fracture mode is not present), the cutting (F_c) and thrust (F_t) forces for a specific position (x, y) in the cutting surface can be calculated as (Liao and Axinte, 2016):

$$F_c(x, y) = \tau(x, y) \frac{w}{N_y} h \csc \phi(x, y) \cos(\lambda(x, y) - \alpha) \sec[\phi(x, y) + \lambda(x, y) - \alpha] \quad (4)$$

$$F_t(x, y) = \tau(x, y) \frac{w}{N_y} h \csc \phi(x, y) \sin(\lambda(x, y) - \alpha) \sec[\phi(x, y) + \lambda(x, y) - \alpha] \quad (5)$$

where h is the depth of cut, α the rake angle, λ the friction angle (where

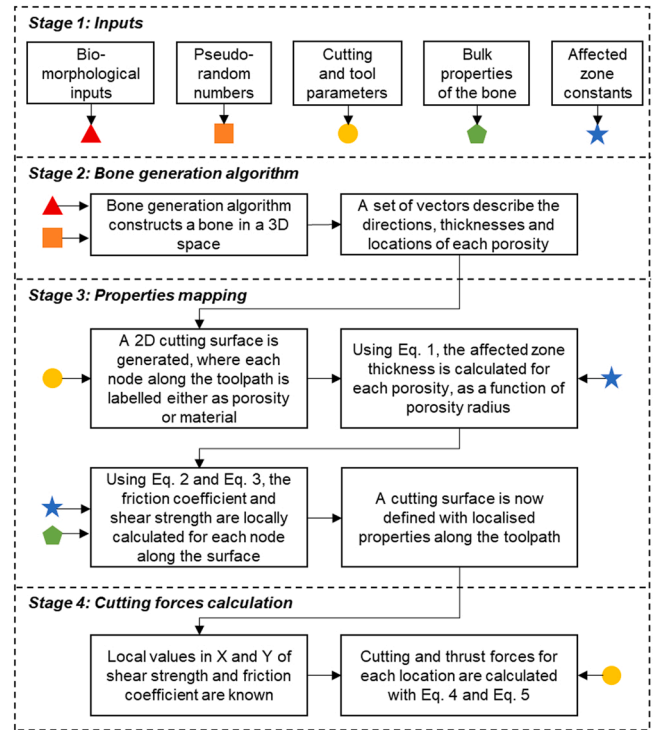


Fig. 5. Flowchart of the cutting forces model. After a set of inputs are fed to the program, a bone is constructed, and depending on the cutting direction relative to the bone structure, a cutting surface is generated. A properties mapping is performed on each node of the surface using the affected zone constants, and the cutting and thrust forces are then calculated for each position along the toolpath.

$\lambda(x, y) = \arctan \mu(x, y)$) and, due to the plane-strain conditions, the Ernst-Merchant relationship, $\phi(x, y) = \frac{1}{4}(\pi - 2\lambda(x, y) + 2\alpha)$ (Shaw, 2005), can be assumed. Additionally, w/N_y represents the size of the discrete element in the Y direction. This way, for a specific position along the tool path (i.e., for any given x), the total cutting forces can be calculated as the summation of all the elemental forces along y .

2.2. Proof that internal irrigation has an influence in the cutting mechanism of ex-vivo bone

Since orthogonal cutting represents a plane-strain condition for forces analysis, it was chosen to study and validate the cutting forces model here proposed. Mid-diaphysis from a bovine femur were used in this research due to its similarities with human bone at the macro- and microscale in terms of architecture, composition, healing capabilities, apparent density, mineral content, elastic modulus, ultimate strength (Liebschner, 2004; Pearce et al., 2007), its mechanical response to machining, and the fact that it allows to perform histological analysis for machining-induced necrosis (Robles-Linares et al., 2021). The bone was acquired from a local butcher and all samples were immediately prepared for machining experiments following a previous research method (Liao and Axinte, 2016), producing final bone shapes of $35 \times 4 \times 4 \text{ mm}^3$ with a cutting section on their top of surface of $12 \times 1.25 \times 1.25 \text{ mm}^3$. All machining trials were conducted in a CNC milling machine (110 PCNC Tormach) with the experimental setup shown in Fig. 2. When not in use, samples were kept in a saline-soaked gauze at -80°C .

A 2-mm solid carbide cutting edge with rake angle of 8° , clearance angle of 8° and nose radius of $1 \mu\text{m}$ was used in this investigation, conducting the orthogonal cutting process at depths of cut of 10, 30 and $50 \mu\text{m}$ to ensure that the bone is not under fracture cutting regime (Liao and Axinte, 2016), and enabling a continuous chip. Additionally, these depths of cut were selected as they cover the usual range that surgical tools, such as drills, see during surgery (Feldmann et al., 2017). All tests were done at room temperature and at constant cutting speed of 3 m/min (e.g. representative of a 2 mm drill at 500 rpm). Additionally, cutting was conducted along the three principal cutting directions (i.e., parallel, across, transverse) relative to the osteons' main orientation (see Table 1). Both internal irrigation (i.e., with the fluid pumping system enabled using sodium chloride 0.9 % as the fluid to mimic interstitial fluid) and dry (i.e., without the fluid pumping system enabled) conditions were employed, with the first being used for the model validation, and the second for comparisons of chip formation mechanism and damage assessment.

Since the DOC was kept below the threshold for fracture cutting mode, a continuous chip was obtained in all tests and for both fluid conditions, where plastic deformation dominated the process. A high-speed camera (IDT Y4-S2 Motion Pro), which enabled chip formation mechanism visualisation confirmed this, where as shown in Fig. 6, even at the largest DOC ($h = 50 \mu\text{m}$), a continuous chip can be identified for both dry (Fig. 6a) and irrigated (Fig. 6b) conditions.

The example shown in Fig. 6 corresponds to cutting along the transverse direction of cortical bone; however, the same behaviour was identified for most of the experiments. In dry conditions, the chip formation mechanism remains similar to what has been reported in previous studies (Bai et al., 2020; Feldmann et al., 2017; Liao and Axinte, 2016). Especially in the case shown in Fig. 6a, the dry chip follows a continuous curling trajectory due to the shear-crack cutting mechanism that takes place at such depth of cut. Nevertheless, when the same machining parameters are used in an internally irrigated bone sample, the chip formation mechanism is altered drastically. The moisturising effect of the fluid upon the chip and in the cutting zone produces a chip that tends to flow parallel to the rake face instead of curling forwards, whereby adherence takes place between the chip and the rake face.

Table 1
Selected orthogonal cutting conditions for the model validation.

Fluid condition	DOC, h , (μm)	Feed direction	Cutting speed (m/min)	Repetitions
Dry (D)	10, 30, 50	Parallel, across, transverse	3	5
Internal irrigation (I)	10, 30, 50	Parallel, across, transverse	3	5

While this was the dominant chip formation mechanism and chip flow direction due to internal irrigation of the bone, there were a minority of cutting tests in which the chip curled onwards.

However, even though internal irrigation drastically affects the chip formation mechanism, there is still the question of its effect on the cutting forces. To investigate this, the cutting and thrust forces were directly measured with a dynamometer (Kistler 9,317 C) at a 10 kHz acquisition rate, thereby allowing to calculate the mean values of shear strength and friction coefficient, as depicted in Table 2. In all instances, the internal irrigation condition produces lower values of both cutting and thrust forces, which implies that less amount of energy is required to enable the shearing or shear-cracking mechanism in the chip formation process. Inherently, this is since the shear strength and friction coefficient along the tool path are significantly lower in the irrigated condition than in the dry state.

Because the interstitial fluid acts as a lubricant in the tool-chip interface, the mean cutting forces are significantly reduced if compared to dry cutting. Generally, as shown in Table 3, the cutting forces for all DOC and directions were within 6 % and 28 % lower when cutting in the internally irrigated state. This difference was more drastic in the thrust force, producing a difference between 13 % and 52 %. The shear strength proved to be 2–18 % lower, which is not as noticeable as in the friction coefficient, which ranged between 6 % and 43 % lower. Besides the average cutting and thrust forces being lower, it is important to note that their standard deviation values also decrease (see Table 2). In this case, the standard deviation can be considered to represent the amplitude variation of the waveform of force. Thus, it can be concluded that the force variation is much lower (up to 70 % in the cutting force and up to 63 % in the thrust force) in internally irrigated bone than in dry bone. This, in line with the observed chip formation processes, highlights that the interstitial fluid increases the apparent ductility due to the moisturising or softening effect, thereby producing a smoother chip flow with lower and more constant values of force.

The internal irrigation condition during cutting has much more impact in the thrust force and in the friction coefficient, whereas less effect is seen on the cutting force and the shear strength. This can be explained by analysing the fluid effect upon the chip flow. The fluid that gets trapped within the chip then gets in contact with the rake face and produces a significantly lower amount of friction (up to 54 % lower friction force), which enables a smooth chip flow (as shown in Fig. 6b). Additionally, the friction force runs only with an 8° misalignment from the thrust force direction (i.e., runs along the rake face). This, in line with the fact that the normal force on the rake face is less affected (only up to 19 % reduction) and has a greater mismatch in orientation with the cutting force direction is the reason why the thrust forces are more significantly affected (in terms of percentage reduction) than the cutting forces. Additionally, this is also a result of the lower friction angle that is obtained due to the fluid presence.

Since there are evident differences between bone cutting in dry and irrigated state, this implies that traditional bone cutting models could be adapted to consider the effect of the fluid-filled porosities. Such a model has been presented in the previous section and an example of the cutting forces compiled with Eqs. (2)–(5) are compared with the experimental measurements in Fig. 7 for the case of internal irrigation condition.

In general, the model can produce comparable forces to those obtained experimentally (Fig. 7a,d,g) not only regarding the mean values of the force, but also in how the forces vary along the toolpath. For all cutting directions and DOC, the cutting forces obtained with the model are less than 3 % larger than those from the experimental results. However, the variability of the forces always increases with the DOC, which is expected to occur due to the larger volume of bone being cut. Nevertheless, the thrust force is less accurate in the model, depicting a difference of up to 18 % with experimental results and a minimum of 6 %. This might be since for all directions and DOC the cutting forces are positioned in a 22.8 N window while the thrust forces in a 4.3 N window, thereby increasing the sensibility of the thrust force over the

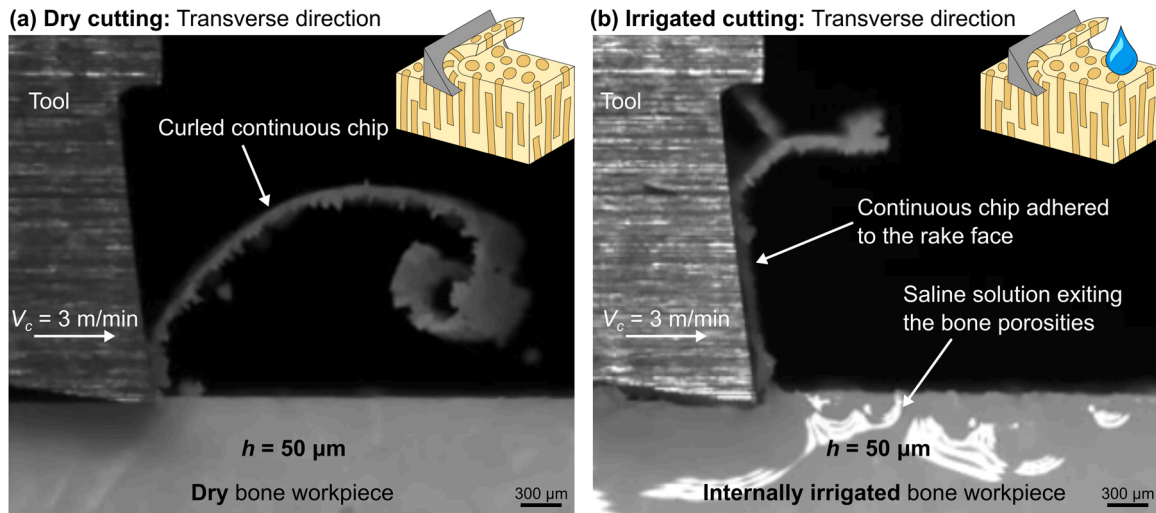


Fig. 6. Chip formation mechanism in dry vs. irrigated conditions at 50 μm of DOC. (a) Dry cutting depicts the expected shear-crack cutting (SCC) mode, yielding a continuous chip. (b) Due to the internal irrigation of the bone, lubrication is enhanced, thus altering the cutting mechanism and increasing the adherence of the chip onto the rake face of the tool.

Table 2

Mean experimental values of cutting force, thrust force, shear strength and friction coefficient for all cutting directions, depths of cut and irrigation conditions. D = dry, I = internal irrigation; results are shown as mean ± std dev.

Cutting direction	DOC, h (μm)	Cutting force, F_c (N)		Thrust force, F_t (N)		Shear strength, τ_s (MPa)		Friction coefficient, μ	
		D	I	D	I	D	I	D	I
Parallel	10	7.9 ± 1.4	6.7 ± 0.4	3.9 ± 0.3	2.3 ± 0.1	197 ± 29	190 ± 15	0.71 ± 0.17	0.51 ± 0.03
	30	14.2 ± 2.6	13.4 ± 1.4	4.5 ± 0.6	3.6 ± 0.3	139 ± 33	137 ± 15	0.49 ± 0.09	0.43 ± 0.02
	50	20.7 ± 5.2	18.0 ± 2.5	5.0 ± 1.1	4.3 ± 0.4	132 ± 30	113 ± 18	0.42 ± 0.13	0.40 ± 0.03
Across	10	6.9 ± 2.1	4.9 ± 1.0	3.1 ± 0.9	1.5 ± 0.5	179 ± 31	147 ± 28	0.83 ± 0.12	0.47 ± 0.07
	30	12.7 ± 3.9	11.6 ± 2.8	4.0 ± 1.1	2.9 ± 0.9	126 ± 27	122 ± 31	0.53 ± 0.18	0.41 ± 0.09
	50	17.0 ± 4.2	15.4 ± 4.8	4.1 ± 1.2	3.5 ± 1.1	111 ± 29	96 ± 36	0.49 ± 0.24	0.37 ± 0.08
Transverse	10	7.5 ± 1.3	6.5 ± 0.6	2.5 ± 0.3	1.6 ± 0.2	217 ± 28	204 ± 21	0.52 ± 0.12	0.40 ± 0.03
	30	18.9 ± 5.0	15.7 ± 2.0	3.4 ± 0.8	2.3 ± 0.4	212 ± 32	181 ± 27	0.36 ± 0.11	0.30 ± 0.04
	50	27.9 ± 6.1	22.8 ± 3.6	3.8 ± 1.1	2.7 ± 0.6	195 ± 34	162 ± 30	0.30 ± 0.07	0.27 ± 0.04

Table 3

Comparison of irrigated (I) and dry (D) conditions, regarding the cutting forces, thrust forces, shear strength and friction coefficient.

Cutting direction	DOC, h (μm)	Reduction of Irrigated (I) condition vs. Dry (D) condition			
		Cutting force, F_c	Thrust force, F_t	Shear strength, τ_s	Friction coefficient, μ
Parallel	10	-15%	-41%	-4%	-28%
	30	-6%	-20%	-2%	-14%
	50	-13%	-13%	-14%	-6%
Across	10	-28%	-52%	-18%	-43%
	30	-9%	-28%	-4%	-23%
	50	-9%	-15%	-14%	-24%
Transverse	10	-14%	-37%	-6%	-23%
	30	-17%	-31%	-15%	-16%
	50	-18%	-30%	-17%	-10%

cutting force by approximately five times.

In the parallel cutting direction, the osteons are roughly oriented with the feed direction, which implies that longitudinal porosities could be found along the toolpath, as shown in Fig. 7b-c; this consequently produces a force variability that is not as important as in the other cutting directions. For the example shown in Fig. 7a, the mean cutting and thrust forces are essentially equal, even having similar standard deviation.

In the across cutting direction, the osteons run perpendicular to both the cutting and thrust direction, which implies that the axes of the porosities might, at some point, be roughly coincident with the cutting

edge position. This is the reason why when cutting in this direction, the forces depict the largest variation, in some cases going to zero or near-zero values. For instance, the experimental force drops to near-zero values in Fig. 7d near the 2 mm mark due to the large porosity that is shown in Fig. 7e. However, note how the force starts to drop even before the cutting edge gets in contact with the porosity; this is due to the lubricating effect on the friction coefficient and the softening effect on the shear strength in the regions close to the porosity. The same phenomenon takes place in the forces obtained with the model. In the model forces, the force drops near the 3.75 mm mark, and this is due to the porosity shown in Fig. 7f. However, in this case (model) the porosity is

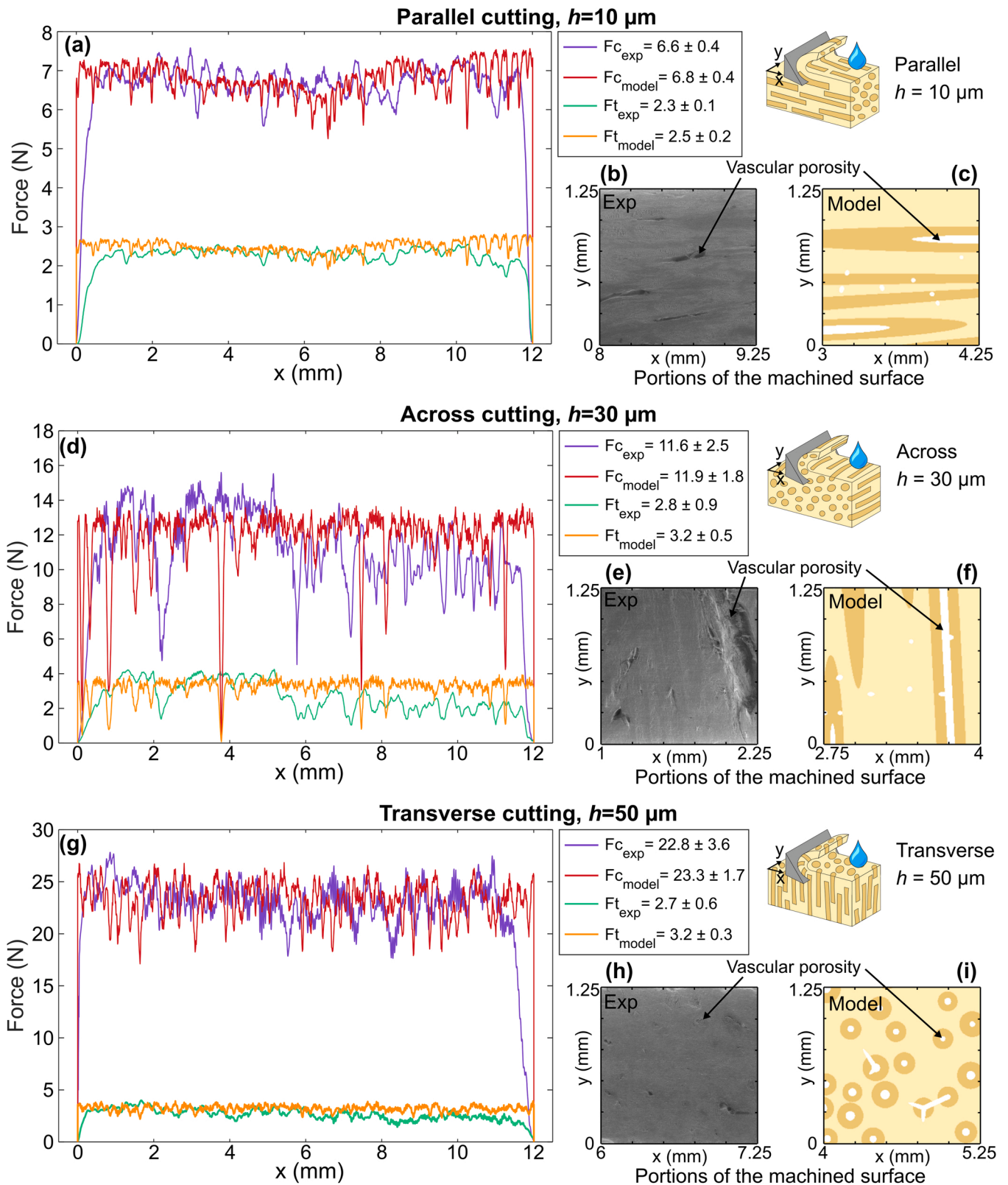


Fig. 7. Examples of cutting and thrust forces for the different cutting directions and depths of cut in internally irrigated machining, as obtained experimentally and via the model. (a-c) Parallel cutting direction with a $10\ \mu\text{m}$ DOC. (d-f) Across cutting direction with a $30\ \mu\text{m}$ DOC. (g-i) Transverse cutting direction with a $50\ \mu\text{m}$ DOC.

significantly smaller than that from Fig. 7e (experiment), which is why the affected zone near the porosity is smaller too, thereby producing a narrower force drop width in comparison.

In the transverse cutting direction, the osteons are parallel to the thrust direction, which is why the largest values of shear stress are expected in this direction as opposed to the other two. In this scenario the force variability is mostly dependent on the osteon density (i.e., number of osteons per unit area) and porosity size, which in this case were measured to be 14.5 osteons per mm^2 , 38–92 μm Haversian porosity diameter and 31–43 μm Volkmann's porosity diameter; these values are in line with literature values (Predoi-Racila and Crolet, 2008; Yan et al., 2006). This inherently results in a set of forces that is not only similar in mean values, but also in the way in which the variability of the force takes place, which is why the experimental force curves shown in Fig. 7g match well with those obtained from the model. Note how the surface shown in Fig. 7h has only a little number of porosities that are visible, while many are visible in the model-obtained surface. This is since the fluid also facilitates surface smearing, which could produce porosity clogging, as it will be discussed next.

Post-machining SEM (FEI Quanta 650) analysis was performed on all samples in low vacuum conditions to assess the surface damage related to the cutting conditions. It is well known that the maximum surface damage is expected with the largest DOC, especially if cutting under the fracture regime (Zhang et al., 2022). However, since the fracture mode was avoided in these experiments, the largest damage occurred when cutting with 50 μm of DOC, as shown in Fig. 8, where the damage is compared between dry and irrigated conditions.

The surface morphology when cutting in dry state appears more damaged with tissue tearing and material drag, especially in regions close to the porosities. For instance, in Fig. 8a, portions of a Haversian porosity and a Volkmann's canal can be properly appreciated, but material in the edges of the porosity exhibits strong signs of material drag. Moreover, the material drag was enough to push a portion of the osteon onto the open porosity. In Fig. 8b, the osteon was cut on its upper portion, meaning that only a small portion of the porosity was cut through with the cutting edge; this resulted in a collapsed osteon with breakage in multiple zones near the porosity. In this case, material drag and tearing occurred simultaneously along the cutting edge when passing through the osteon, which is due to the parallel alignment of the collapsed osteon with the cutting tool; this is the reason why most of the surface exhibits signs of damage. In the transverse cutting direction (Fig. 8c), most of the surface surrounding the Haversian canals depict signs of material drag and large porosities seem collapsed, which could be explained due to the high forces required in this direction and the ease of collapsing due to the lack of fluid within. When the cutting is produced in the internally irrigated state, the surface morphology changes drastically, appearing smooth and almost defect-free, even for the largest value of DOC (i.e., 50 μm), which is shown in Fig. 8d-f. An interesting effect in this case is that the fluid response on the material can be appreciated not only in terms of lower forces, as it has been shown previously, but also in terms of surface smearing. The fluid from the porosities acts as a lubricant, meaning that the tool-material interaction is less aggressive, and in turn, the machined surface is smooth. For instance, when comparing Fig. 8d with Fig. 8a, material drag is essentially non-existent; but in lieu of this, the majority of the porosities appear to be partially clogged. This might occur due to the possible material smearing or redeposition that is facilitated due to the stickiness of the material in regions near the porosities. However, in the presence of larger porosities (as that in Fig. 8e), the lower forces are safe enough to avoid the porosities from collapsing, and the evident material damage near the porosities in dry state (Fig. 8b) is difficult to be enabled. This could explain why open porosities exhibit smooth surfaces around them if machined in internally irrigated state. Similar signs of minimum damage are shown in Fig. 8f in the transverse cutting direction where most of the Haversian canals appear partially clogged due to a superficial layer of smeared material, which was enabled due to the soft

material surrounding the fluid-filled porosities. Nevertheless, those porosities that are open, still shown signs of minimum damage with mostly smooth surfaces around.

To produce a more comprehensive analysis of surface damage (in terms of morphology), the surface roughness was assessed. 3D inspection of the machined surfaces was completed using the Bruker Alicona InfiniteFocus G3 and MountainsMap Premium software. This was achieved by non-contact probing by focus variation which allowed for measurements of the surface morphology for all the cutting directions (Fig. 9).

Simple comparative inspection of Fig. 9 highlights that the roughest surfaces were obtained under dry cutting conditions, especially in the across cutting direction (Fig. 9b). It is important to note that the colour scale considers the depth of the vascular porosities, meaning that the deepest portions in each image correspond not to a machining-induced defect, but to the natural porosity that is located there. In the case of dry machining (Fig. 9a-c), regions surrounding the porosities exhibit the largest values of roughness and while this is still true in internally irrigated machining (e.g., Fig. 9d,f), it is not the exclusive case, since very smooth near-porosity surfaces can also be obtained, as shown in Fig. 9e when cutting in the across direction.

The mean values of the area surface roughness (S_a) corresponding to the surfaces shown in Fig. 9 are listed below in Table 4. However, making an objective comparison based solely on Fig. 9 or on the S_a values is largely misleading, as these consider the porosity voids as a change in the roughness. To tackle this, three linear measurements of surface roughness (R_a) were averaged for each sample along the cutting direction in positions where no porosities could be encountered, as so to get a roughness value that would correspond only to the real machined surface, thereby removing the uncertainty caused by the contribution of the porosity voids into the area surface roughness (S_a). In the parallel cutting direction, the surface roughness (R_a) decreases from 0.241 μm to 0.199 μm (–17 %) when shifting from dry to internally irrigated machining. Similarly, in the across and transverse directions the roughness are 34 % and 19 % lower, respectively. This proves that the internal irrigation in the bone produces significant changes in the surface morphology and roughness post-machining.

An interesting result, however, is that the across cutting direction produced the roughest surface (Table 4) amongst the three directions. This is not expected as usually the transverse direction exhibits more signs of damage and roughness (Zhang et al., 2022). The reason for this might be traced back to the experimental results of cutting and thrust forces shown in Table 2, where even when largest values of shear stress and cutting forces were obtained for the transverse direction, the friction coefficient in the across direction was measured to be larger than in the transverse direction. Thus, the larger signs of damage that were found in the across direction could be due to the increased friction that facilitates material drag and tissue tearing.

Up to now, it has been shown that the internal irrigation condition in the vascular porosities of the bone produces a drastic change in cutting forces, chip formation and surface damage. However, the reason for this is not trivial. Indeed, the simple use of a lubricant will inherently produce these changes in a general machining environment with any material, but the main difference here is that the lubricant is applied internally and through the natural porosities of the bone; somehow resembling what bone machining would be in a more realistic scenario (i.e., surgery). Interestingly, the fluid affects the bone not only in places where the fluid is contained, but it seems that the fluid has a “reach” capacity that results in lower friction coefficient and lower shear strength, locally, in regions of the bone (i.e., osteon, interstitial lamella) that are within a threshold distance of the vascular porosity. However, the possible explanation for this softening or moisturising effect near the porosities relies on the porosity systems that exist in the bone and their permeability capacities.

While the overall porosity of bone is usually attributed to the vascular porosity (VP) system (i.e., Haversian and Volkmann's canals)

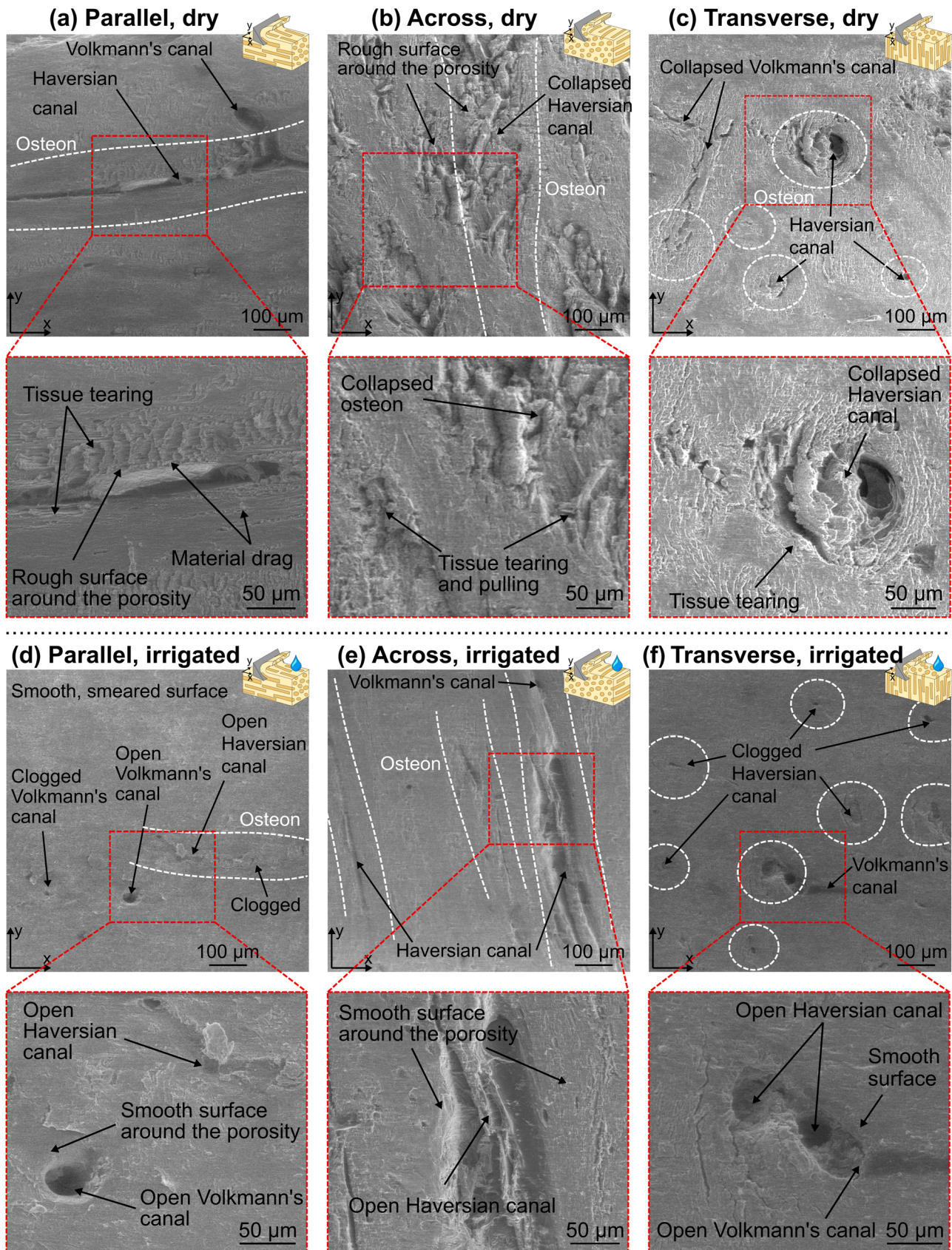


Fig. 8. Comparison of post-machining surface damage with $h = 50 \mu\text{m}$ via SEM inspection. (a-c) Machined surfaces produced with dry cutting; severe damage and tissue tearing is visible, especially in regions near the porosities. (d-f) Machined surfaces produced with internal irrigation; smooth surfaces and smearing are visible. Material near open porosities remains mostly smooth.

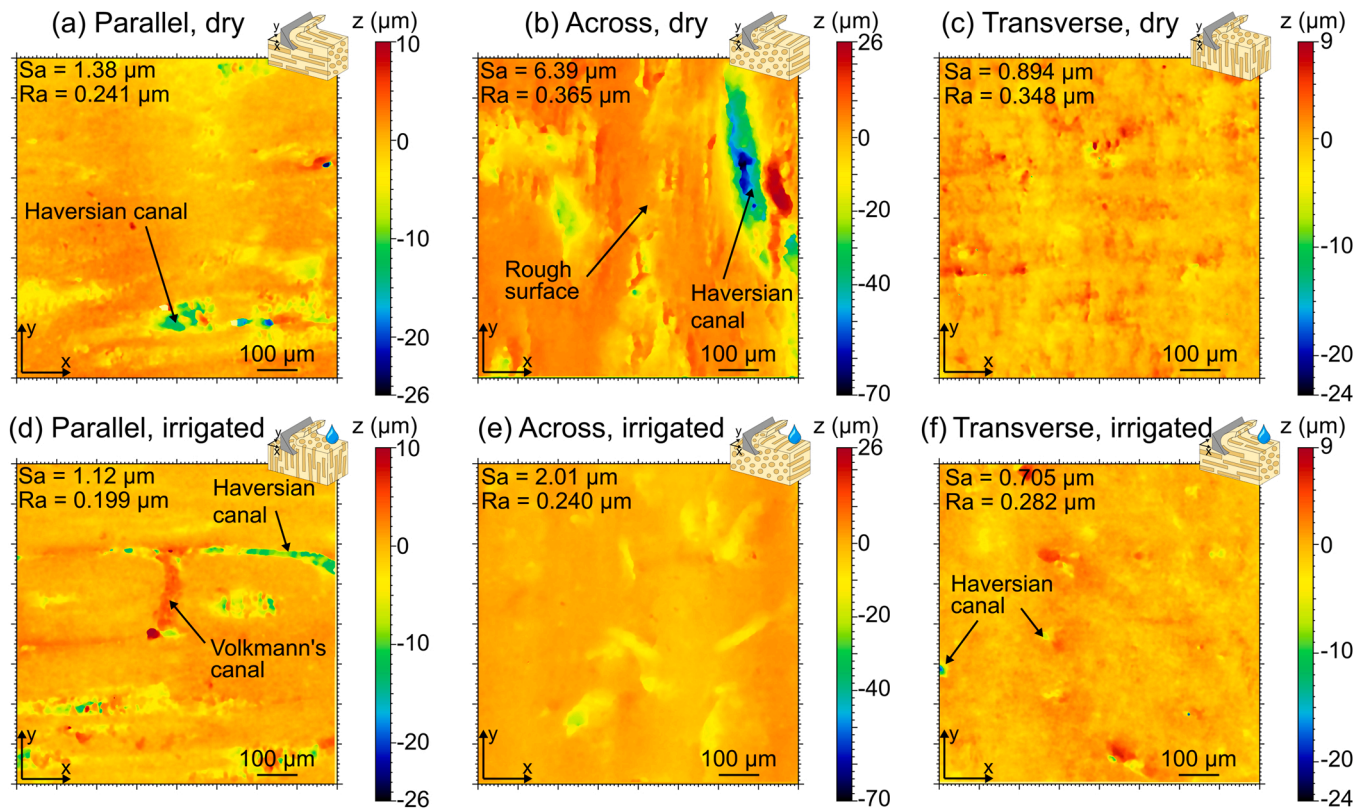


Fig. 9. Representative comparison of post-machining surface scans with $h = 50 \mu\text{m}$ DOC. (a-c) Machined surfaces produced with dry cutting. (d-f) Machined surfaces produced with internal irrigation. Note how the roughness values are largely affected by the porosities in the surface.

Table 4

Post-machining surface roughness with $h = 50 \mu\text{m}$. Due to porosities of the bone microstructure, the area surface roughness (S_a) depicts larger values than what the machined surface realistically is. Therefore, linear measurements of surface roughness (R_a) were taken in non-porous locations too. D = dry, I = internal irrigation.

Direction	Fluid condition	S_a (μm)	R_a (μm)
Parallel	D	1.38	0.241
	I	1.12	0.199
Across	D	6.39	0.365
	I	2.01	0.240
Transverse	D	0.894	0.348
	I	0.705	0.282

due to its large diameter range (40 – 90 μm), there are also two additional porosity systems at the nanometric scale: lacunar-canalicular porosity (LCP), with a diameter range of 50 – 200 nm; and (2) collagen-hydroxyapatite porosity (CAP) with approximately 10 nm in diameter (Cowin and Cardoso, 2015). These porosity systems are interconnected and enable the permeability of the bone from the main VP in the transcortical and intracortical directions via the LCP and CAP (Cardoso et al., 2013). While the LCP and CAP are important for explaining the permeability of bone, the ratio of VP to LCP permeability is in the order of 10^8 and the VP to LCP pore diameter ratio is approximately 167. Nevertheless, due to the low fluid pressure in the VP and the high pressure in the LCP, the latter plays a more significant role in the mechanical behaviour of the tissue (Cowin and Cardoso, 2015). The permeability is able to produce poroelastic changes in the behaviour of bone, meaning that the local dry/irrigated state will exhibit different mechanical properties (Cowin, 1999). Consequently, this justifies why the localised fluid effect can be regarded as it has been previously explained up to now.

In this orthogonal cutting study it has been proven, for the first time,

that internal irrigation is of large importance when it comes to modelling of the cutting forces involved in the process and it has been demonstrated that the solution for this relies on considering a porosity-size-dependent affected region in the bone in which the friction coefficient and the shear strength are decremental due to the permeability of the bone that is enabled from the vascular porosity into the tissue via the LCP and the CAP systems. While it has also been shown that surface morphology and chip formation is drastically affected because of the fluid presence.

3. Non-orthogonal cutting of bone considering the influence of internal irrigation and external cooling

While the previous chapter focused on studying the internal fluid presence effect upon the cutting forces, chip formation mechanism and surface damage, an open question here is if the internal irrigation effect is still significant when applying flood cooling, which is normal practice in surgical conditions. Since the objective of this study is to understand the bone as a material in a “close-to-surgical environment”, flood cooling must also be considered. In a surgical scenario, flood cooling is employed with the primary intention of minimising temperature rise and minimising tissue necrosis. As such, to study the effects of internal irrigation and flood coolant, these same aspects (i.e., temperature and necrosis) are here compared.

Due to the small contact time in orthogonal cutting, heat generation is not easily enabled. Therefore, to assess the effects of the interstitial fluid on heat propagation during machining, another set of cutting trials were performed with fly cutting. To this end, a single straight tooth milling tool (HSS) was employed in the same milling machine tool employed for the orthogonal cutting trials (Fig. 2), and since the objective of these tests was to assess the effect of temperature, two different machining conditions were used, to allow a high (HT) and a low (LT) temperature during the cutting process (Table 5). The samples

Table 5

Selected fly cutting conditions for assessing necrotic damage. A low (LT) and high (HT) temperature set of machining conditions were employed in bone in dry (D), internally irrigated (I), dry with external coolant (DE) and internally irrigated with external coolant (IE) fluid states.

Temperature condition	Fluid condition	Feed direction	Radial DOC (μm)	Cutting speed (m/min)	Feed per tooth (μm)	Repetitions
LT	D, I, DE, IE	Parallel	750	25	30	2
HT	D, I, DE, IE	Parallel	750	100	10	2

were prepared equally as for the orthogonal cutting trials to obtain overall bone samples of $35 \times 4 \times 4 \text{ mm}^3$ with a cutting section on their top of surface of $12 \times 1.25 \times 1.25 \text{ mm}^3$. These were machined only in the parallel direction relative to the osteons since it is a representative feed direction in surgery and because the thermal properties of cortical bone are fairly isotropic (Davidson and James, 2000; Feldmann et al., 2018), thereby enabling the completion of the thermal damage assessment for the scope of this study.

It is well known that thermal measurements in bone machining is challenging (Zhang et al., 2022), but infrared (IR) thermography is capable of providing reliable relative measurements for a given set of machining conditions (Shu et al., 2020). As such, temperature measurements were completed by IR thermography using a FLIR A655SC Long Wavelength IR camera and data was recorded at 50 Hz, as shown in Fig. 10. To record the bone temperature with the IR camera, the emissivity of the bone was set to 0.96 (Feldmann and Zysset, 2016) for all experiments, while locating the camera at approximately 500 mm away from the cutting zone. The data was processed using the ResearchIR Max software by FLIR and MATLAB to calculate the maximum temperatures (T_{max}) for all tests. This was done by averaging the maximum temperature of each frame within the region of interest (i. e., the bone cutting section shown in Fig. 10b), for all the machining conditions (see Table 6).

To assess the thermal damage related to the measured temperatures, a necrotic assessment was performed via histological analysis to all the fly cutting samples. Since more intense thermal fields are expected near the end of the cut, histological analysis was performed at the 9 mm mark of the 12 mm cutting length. The methodology for the necrosis assessment has been done according to a previous work (Robles-Linares et al., 2021). The process consists of a cellular fixation process using 10 % neutral formalin for preserving the cells, a 10-day decalcification process for softening the tissue, a paraffin-mounting process, microtome cutting of the samples to obtain 7- μm bone slices, an haematoxylin and eosin (H&E) staining process to enable improved morphological observation of the tissue (i.e., easy identification of the osteocytes) and, finally, mounting the stained slices in a mixture of distyrene, plastic and xylene (i.e., DPX) in microscopy slides. The slides are then analysed with light microscopy (see Fig. 11). Image analysis and necrotic depth evaluation (i.e., measurement from the cut surface to the disappeared

Table 6

Necrotic damage as measured with histological analysis for all the fly cutting samples. LT = low temperature drilling, HT = high temperature drilling, D = dry, DE = dry with external cooling, I = internal irrigation, IE = internal irrigation with external cooling.

Temperature condition	Fluid condition	Maximum temperature T_{max} ($^{\circ}\text{C}$)	Necrotic depth (μm) mean \pm std dev
LT	D	47.6	40.2 ± 3.4 (n = 63)
	DE	22.3	0
	I	38.1	18 ± 2.9 (n = 54)
	IE	20.8	0
HT	D	65.2	56 ± 5.7 (n = 55)
	DE	23.1	0
	I	57.9	37 ± 4.2 (n = 49)
	IE	22.2	0

osteocytes extent) were made manually in Fiji (ImageJ). A total of 9 slices per sample were inspected, making at least 5 distance measurements on each of them.

These experimental conditions confirmed that larger temperatures usually produce deeper necrotic depths, but that internal irrigation plays a determining role in terms of heat dissipation and necrotic damage (see Table 6). For instance, when cutting under high temperature (HT) conditions in a fully dry (D) bone state (i.e., without internal irrigation and without external coolant) the maximum temperature was measured to be $65.2 \text{ }^{\circ}\text{C}$, which, in terms of necrosis was translated to be $56 \pm 5.7 \text{ }\mu\text{m}$ (n = 55). It is important to note that these were the maximum values of both temperature and necrosis of all experiments, as it was expected. With internally irrigated (I) bone, the same set of machining parameters (HT) produced a temperature of $57.9 \text{ }^{\circ}\text{C}$ with a $37 \pm 4.2 \text{ }\mu\text{m}$ (n = 49) necrotic depth, which proves that interstitial fluid within the vascular porosities of the bone has the capability of heat dissipation, thereby producing lower levels of thermal fields and necrosis. This might be explained by analysing the mediums of heat transfer in dry and irrigated conditions. In dry machining, the porosities could be regarded as air-filled spaces that act as poor thermal conductors since air has a very low thermal conductivity (0.026 W/mK (Stephan and Laesecke, 1985) at room temperature and atmospheric pressure), thereby

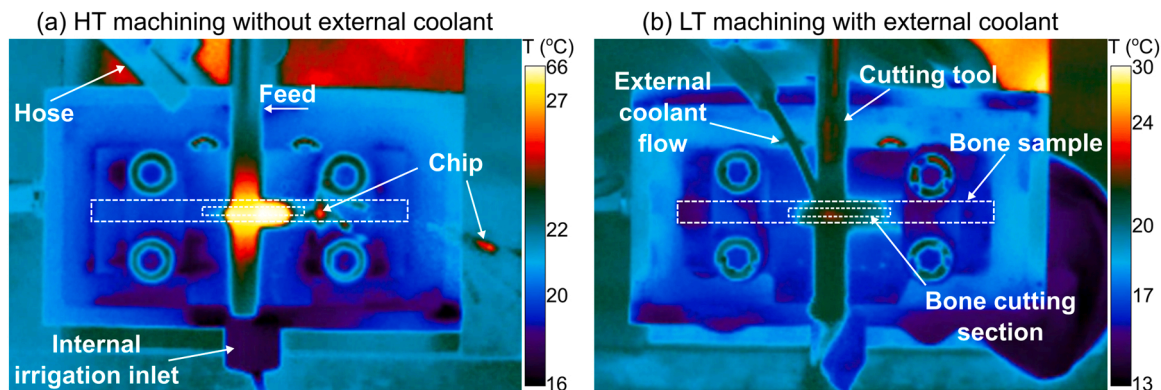


Fig. 10. Infrared thermography measurements examples for the maximum and minimum temperature scenarios obtained throughout all the experiments. (a) High temperature (HT) machining without external coolant and in dry (D) state. (b) Low temperature (LT) machining with internal irrigation and external coolant delivery (IE).

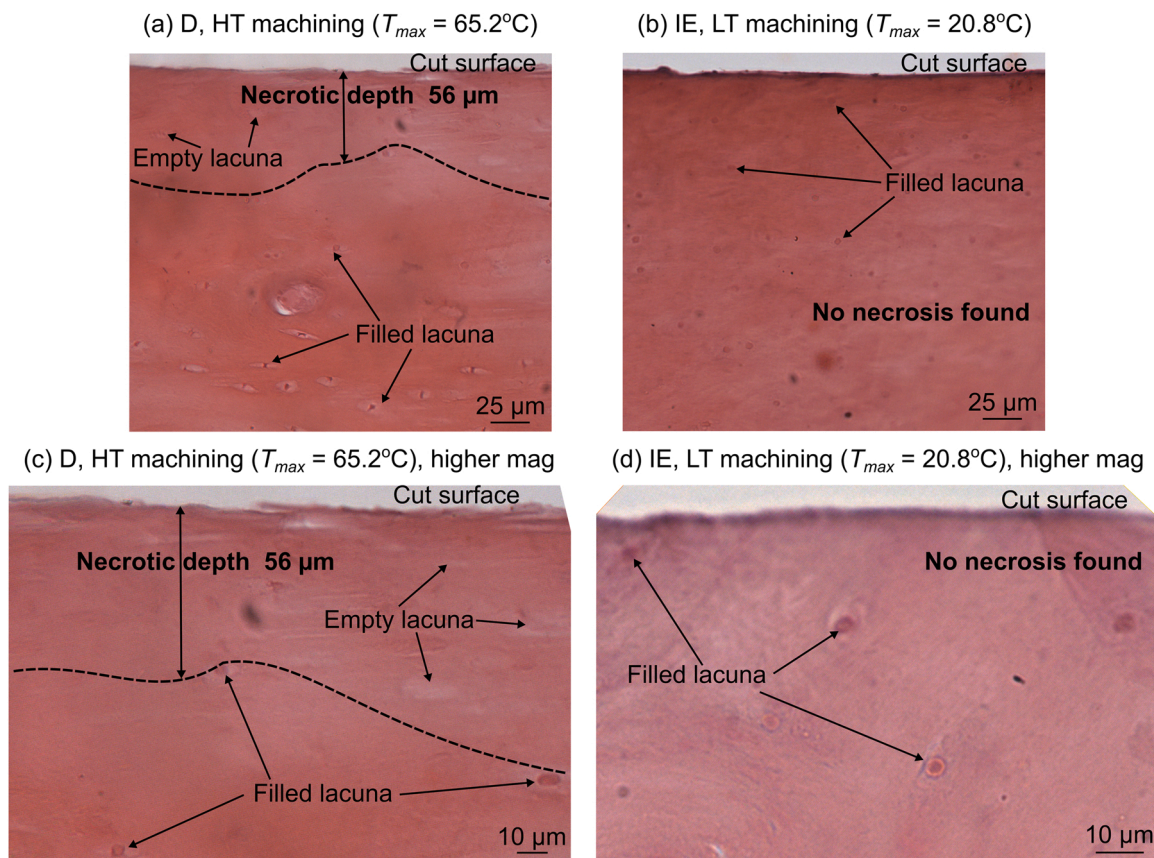


Fig. 11. Necrosis assessment with histological analysis on the bone subsurface following fly cutting. (a,c) High temperature (HT) machining in dry (D) conditions, where the maximum temperature and necrosis were measured as 65.2 °C and $56 \pm 5.7 \mu\text{m}$ ($n = 55$), respectively. (b,d) Low temperature (LT) machining in internally irrigated and external coolant (IE) conditions, where no necrosis was found.

hindering heat propagation into the bone and facilitating heat concentration in the tool-chip interface, which in parallel with bone's low thermal diffusivity (Feldmann et al., 2018) is why it is expected to have heat concentration in the tool-chip interface in bone cutting (Feldmann et al., 2017). However, in internally irrigated machining, the porosities are filled with interstitial fluid, which in this case has been mimicked by employing saline solution, fluid that possesses superior conductivity (0.594 W/mK (Ozbek and Phillips, 1980)) over air and therefore could be expected to conduct heat at a faster rate away from the cutting zone, which is translated into lower temperatures and, therefore, less necrotic damage.

In low temperature (LT) machining of bone in dry (D) state, the maximum temperature was measured to be 47.6 °C, which is 17 °C lower than that achieved with high temperature (HT) machining parameters. In this case (LT, D), the temperature produced a $40.2 \pm 3.4 \mu\text{m}$ ($n = 63$) necrotic depth, which is significantly lower than the 56 μm measured on its HT-machined counterpart (HT, D). However, it is interesting to note that even if a larger temperature (57.9 °C) was measured for the internally irrigated sample (HT, I) over the LT, D sample (47.6 °C), it displayed slightly less necrotic damage (37 μm vs. 40.2 μm, respectively). The reason for this is related to the employed machining parameters. Cutting with HT machining parameters, while producing larger thermal fields, also reduces the cutting time to 75 %, as opposed to the LT parameters that yield lower thermal fields but with an increased time window for the cutting process to take place. This inherently creates a compromise of the time-temperature relation that affects the response of the cells to thermal damage (Augustin et al., 2008) by increasing the time in which lower temperatures are being held within the tissue.

The use of external coolant in both HT and LT machining conditions

produced no necrotic damage. As expected, this is due to the intense heat dissipation that is provided by the external fluid, but it should be noted that if more aggressive machining conditions (i.e., in terms of heat generation) were employed, necrosis could be present even while using external cooling solutions.

4. Conclusion

Bone cutting is a complex material for machining analysis since it comprises both a material with an intricate hierarchical microstructure and a living tissue with embedded cells. Typically, bone cutting research is conducted ex-vivo and in a dry state; thereby creating a scenario fully out of the natural environment of bone. This type of studies, while useful, have neglected the effects that blood and interstitial fluid in the vascular porosities may have upon the chip formation mechanism, cutting forces and thermal and mechanical damages. Therefore, in this work, the mechanical behaviour of cortical bone was studied in conditions closer to a surgical scenario by enabling fluid flow through the vascular channels of the tissue during machining, aspect that has so far been neglected.

With a series of orthogonal cutting trials, it was found that internal irrigation affects the cutting and thrust forces by reducing them by up to 28 % and 52 %, respectively, which is attributed to the lower apparent values of shear strength and friction coefficient (up to 18 % and 43 % lower, respectively) that are produced due to the presence of fluid. It was also found that while severe mechanical damage is produced in dry cutting, internal irrigation produces smoother surfaces with less porosity collapse and increased smearing capability.

The localised effect of fluid-filled porosities was studied with orthogonal cutting, and it was found that the bone material surrounding

each individual porosity suffers from a softening effect that is size dependent upon the porosity diameter. In the porosity wall, the shear strength is approximately 50 % lower than its bulk value, while the friction coefficient is about 8 % lower. Nevertheless, these values linearly increase back to their bulk value in an annular zone surrounding the porosity that is confined to 1.6 times the porosity diameter for the case of shear strength, but 2.2 times in the case of friction coefficient.

A mathematical model was developed considering the microstructure's randomness and the gradient of properties (i.e., shear strength, friction coefficient) in near-porosity sites along the toolpath. This enabled the calculation of cutting and thrust forces and it was demonstrated that the model is capable of not only producing significantly similar mean values of force (3–18 % error) when compared to experimental data, but also its variability along the cut. Here, it has been demonstrated that both the porosity randomness and the properties gradients near the porosities play a major role in modelling the variability of cutting forces in orthogonal cutting of cortical bone. Besides allowing for accuracy in cutting forces predictions, the model also serves the purpose of predicting the variation of forces in near-porosity sites due to the gradient of properties that takes place because of internal irrigation.

The effect of internal irrigation was also assessed in terms of necrotic damage with fly cutting trials that enabled heat generation. It was found that dry cutting exhibited the largest signs of necrosis, and that internal irrigation is capable of increasing heat dissipation significantly, thereby producing lower levels of necrosis of up to 55 % lower than dry cutting. It was also confirmed that the use of external coolant released the tissue of any necrotic damage, thereby proving the importance of always employing external coolant in surgery.

This bone machining study shows, for the first time, that interstitial fluid within the porosities of the bone produces a drastically different machining behaviour in terms of forces, mechanical damage and necrosis, as compared to the traditional state in which bone cutting is studied (i.e., dry condition). This was found to occur due to the reduced friction coefficient and shear strength of the bone, especially in localised portions of the tissue near the porosities. Furthermore, it is believed that this material behaviour should exist under surgical conditions in the absence of external coolant delivery.

While this research is limited to ex-vivo bone and saline solution playing the role of interstitial fluid, it aids to minimise the gap between bone machining research and surgical practice (e.g., orthopaedics, dentistry). For instance, the model here presented can straightforwardly be applied patient-specifically, for example, using computerised tomography (CT) to obtain the microstructural distribution of the patient. This could then be employed to predict the cutting forces (and therefore expected damage) of a fixed set of machining conditions or inversely be modified to calculate the necessary machining parameters to not exceed a threshold force.

Funding

This work was supported by The University of Nottingham, the Mexican National Council for Science and Technology (CONACYT) and the Nottingham Research Fellowship programme.

CRediT authorship contribution statement

Jose A. Robles-Linares: Conceptualisation, Methodology, Validation, Formal analysis, Investigation, Data curation, Writing – original draft, Writing – review & editing, Visualisation. **Zhirong Liao:** Conceptualisation, Methodology, Supervision, Writing – review & editing. **Dragos Axinte:** Conceptualisation, Methodology, Visualisation, Supervision, Funding acquisition, Writing – review & editing, Project administration. **Andres Gameros:** Conceptualisation, Methodology, Supervision, Writing – review & editing.

Declaration of Competing Interest

The authors declare that they have no known competing financial interests or personal relationships that could have appeared to influence the work reported in this paper.

Data Availability

All data needed to evaluate the conclusions of the paper are present in the paper. Additional data related to this paper may be requested from the authors.

Acknowledgments

The authors thank Mr. I. Ward from the School of Life Sciences, University of Nottingham for his advice regarding tissue processing. The authors thank the Nanoscale and Microscale Research Centre (nmRC) for providing access to instrumentation.

References

- Augustin, G., Davila, S., Mihoci, K., Udiljak, T., Vedrina, D.S., Antabak, A., 2008. Thermal osteonecrosis and bone drilling parameters revisited. *Arch. Orthop. Trauma Surg.* 128, 71–77. <https://doi.org/10.1007/s00402-007-0427-3>.
- Bai, W., Shu, L.M., Sun, R.L., Xu, J.F., Silberschmidt, V.V., Sugita, N., 2020. Mechanism of material removal in orthogonal cutting of cortical bone. *J. Mech. Behav. Biomed. Mater.* 104. <https://doi.org/10.1016/j.jmbm.2020.103618>.
- Baro, D.K., Deoghare, A.B., 2018. Investigation of cutting force and temperature variation in orthogonal cutting of cortical bone. *Mater. Today Proc.* 5, 12595–12608. <https://doi.org/10.1016/j.matpr.2018.02.242>.
- Cardoso, L., Fritton, S., Gailani, G., Benalla, M., Cowin, S., 2013. A review of recent advances in the assessment of bone porosity, permeability, and interstitial fluid flow. *J. Biomech.* 46, 253–265. <https://doi.org/10.1016/j.jpe.2011.02.012>.
- Chen, Z.H., Zhang, Y., Wang, C.Y., Chen, B., 2021. Understanding the cutting mechanisms of composite structured soft tissues. *Int. J. Mach. Tools Manuf.* 161, 103685. <https://doi.org/10.1016/j.ijmactools.2020.103685>.
- Childs, T.H.C., Arola, D., 2011. Machining of cortical bone: simulations of chip formation mechanics using metal machining models. *Mach. Sci. Technol.* 15, 206–230. <https://doi.org/10.1080/10910344.2011.580699>.
- Cowin, S.C., 1999. Bone poroelasticity. *J. Biomech.* 32, 217–238. [https://doi.org/10.1016/S0021-9290\(98\)00161-4](https://doi.org/10.1016/S0021-9290(98)00161-4).
- Cowin, S.C., Cardoso, L., 2015. Blood and interstitial flow in the hierarchical pore space architecture of bone tissue. *J. Biomech.* 48, 842–854. <https://doi.org/10.1016/j.jbiomech.2014.12.013>.
- Currey, J.D., 2002. *Bones: Structure and Mechanics*, first ed. Princeton University Press, New Jersey.
- Davidson, S.R.H., James, D.F., 2000. Measurement of thermal conductivity of bovine cortical bone. *Med. Eng. Phys.* 22, 741–747. [https://doi.org/10.1016/S1350-4533\(01\)00003-0](https://doi.org/10.1016/S1350-4533(01)00003-0).
- Feldmann, A., Zysset, P., 2016. Experimental determination of the emissivity of bone. *Med. Eng. Phys.* 38, 1136–1138. <https://doi.org/10.1016/j.medengphy.2016.06.019>.
- Feldmann, A., Anso, J., Bell, B., Williamson, T., Gavaghan, K., Gerber, N., Rohrbach, H., Weber, S., Zysset, P., 2016. Temperature prediction model for bone drilling based on density distribution and in vivo experiments for minimally invasive robotic cochlear implantation. *Ann. Biomed. Eng.* 44, 1576–1586. <https://doi.org/10.1007/s10439-015-1450-0>.
- Feldmann, A., Ganser, P., Nolte, L., Zysset, P., 2017. Orthogonal cutting of cortical bone: Temperature elevation and fracture toughness. *Int. J. Mach. Tools Manuf.* 118–119, 1–11. <https://doi.org/10.1016/j.ijmactools.2017.03.009>.
- Feldmann, A., Wili, P., Maquer, G., Zysset, P., 2018. The thermal conductivity of cortical and cancellous bone. *Eur. Cells Mater.* 35, 25–33. <https://doi.org/10.22203/eCM.v035a03>.
- Hage, I.S., Hamade, R.F., 2013. Micro-FEM orthogonal cutting model for bone using microscope images enhanced via artificial intelligence. *Procedia CIRP* 8, 385–390. <https://doi.org/10.1016/j.procir.2013.06.121>.
- Hancox, N.M., 1972. *Biology of Bone*, first ed. Cambridge University Press, Cambridge.
- Heřt, J., Fiala, P., Petřtýl, M., 1994. Osteon orientation of the diaphysis of the long bones in man. *Bone* 15, 269–277. [https://doi.org/10.1016/8756-3282\(94\)90288-7](https://doi.org/10.1016/8756-3282(94)90288-7).
- Hillery, M.T., Shuaib, I., 1999. Temperature effects in the drilling of human and bovine bone. *J. Mater. Process. Technol.* 92–93, 302–308. [https://doi.org/10.1016/S0924-0136\(99\)00155-7](https://doi.org/10.1016/S0924-0136(99)00155-7).
- Jacobs, C., Pope, M., Berry, J., Hoaglund, F., 1974. A study of the bone machining process - orthogonal cutting. *J. Biomech.* 7, 131–140.
- Karaca, F., Aksakal, B., Kom, M., 2011. Influence of orthopaedic drilling parameters on temperature and histopathology of bovine tibia: an in vitro study. *Med. Eng. Phys.* 33, 1221–1227. <https://doi.org/10.1016/j.medengphy.2011.05.013>.
- Krause, W.R., 1987. Orthogonal bone cutting: saw design and operating characteristics. *J. Biomech. Eng.* 109, 263–271.

- Li, L., Liang, M., Yu, B., Yang, S., 2014. Analysis of thermal conductivity in living biological tissue with vascular network and convection. *Int. J. Therm. Sci.* 86, 219–226. <https://doi.org/10.1016/j.ijthermalsci.2014.07.006>.
- Liao, Z., Axinte, D.A., 2016. On chip formation mechanism in orthogonal cutting of bone. *Int. J. Mach. Tools Manuf.* 102, 41–55. <https://doi.org/10.1016/j.ijmactools.2015.12.004>.
- Liao, Z., Axinte, D., Gao, D., 2019. On modelling of cutting force and temperature in bone milling. *J. Mater. Process. Technol.* 266, 627–638. <https://doi.org/10.1016/j.jmatprotec.2018.11.039>.
- Liao, Z., la Monaca, A., Murray, J., Speidel, A., Ushmaev, D., Clare, A., Axinte, D., M'Saoubi, R., 2021. Surface integrity in metal machining - Part I: fundamentals of surface characteristics and formation mechanisms. *Int. J. Mach. Tools Manuf.* 162, 103687 <https://doi.org/10.1016/j.ijmactools.2020.103687>.
- Liebschner, M.A.K., 2004. Biomechanical considerations of animal models used in tissue engineering of bone. *Biomaterials* 25, 1697–1714. [https://doi.org/10.1016/S0142-9612\(03\)00515-5](https://doi.org/10.1016/S0142-9612(03)00515-5).
- Marco, M., Rodríguez-Millán, M., Santiuste, C., Giner, E., Miguélez, M.H., 2015. A review on recent advances in numerical modelling of bone cutting. *J. Mech. Behav. Biomed. Mater.* 44, 179–201. <https://doi.org/10.1016/j.jmbbm.2014.12.006>.
- la Monaca, A., Murray, J.W., Liao, Z., Speidel, A., Robles-Linares, J.A., Axinte, D.A., Hardy, M.C., Clare, A.T., 2021. Surface integrity in metal machining - Part II: functional performance. *Int. J. Mach. Tools Manuf.* 164, 103718 <https://doi.org/10.1016/j.ijmactools.2021.103718>.
- Ozbek, H., Phillips, S.L., 1980. Thermal conductivity of aqueous sodium chloride solutions from 20 to 330 °C. *J. Chem. Eng. Data* 25, 263–267. <https://doi.org/10.1021/je60086a001>.
- Pearce, A.I., Richards, R.G., Milz, S., Schneider, E., Pearce, S.G., 2007. Animal models for implant biomaterial research in bone: a review. *Eur. Cells Mater.* 13, 1–10. <https://doi.org/10.22203/eCM.v013a01>.
- Predoi-Racila, M., Crolet, J.M., 2008. Human cortical bone: the SiNuPro model: Part I - description and elastic macroscopic results. *Comput. Methods Biomech. Biomed. Engin.* 11, 169–187. <https://doi.org/10.1080/10255840701695140>.
- Robles-Linares, J., Ramírez-Cedillo, E., Siller, H., Rodríguez, C., Martínez-López, J., 2019. Parametric modeling of biomimetic cortical bone microstructure for additive manufacturing. *Mater. (Basel)* 12, 913. <https://doi.org/10.3390/ma12060913>.
- Robles-Linares, J.A., Axinte, D., Liao, Z., Gameros, A., 2021. Machining-induced thermal damage in cortical bone: necrosis and micro-mechanical integrity. *Mater. Des.* 197, 109215 <https://doi.org/10.1016/j.matdes.2020.109215>.
- Robles-Linares, J.A., Winter, K., Liao, Z., 2022. The effect of laser ablation pulse width and feed speed on necrosis and surface damage of cortical bone. *Chin. J. Mech. Eng.* 35, 52. <https://doi.org/10.1186/s10033-022-00740-1>.
- Santiuste, C., Rodríguez-Millán, M., Giner, E., Miguélez, H., 2014. The influence of anisotropy in numerical modeling of orthogonal cutting of cortical bone. *Compos. Struct.* 116, 423–431. <https://doi.org/10.1016/j.compstruct.2014.05.031>.
- Shaw, M.C., 2005. *Metal cutting principles*, second ed. Oxford University Press, New York.
- Shu, L., Sugita, N., 2020. Analysis of fracture, force, and temperature in orthogonal elliptical vibration-assisted bone cutting. *J. Mech. Behav. Biomed. Mater.* 103, 103599 <https://doi.org/10.1016/j.jmbbm.2019.103599>.
- Shu, L., Li, S., Terashima, M., Bai, W., Hanami, T., Hasegawa, R., Sugita, N., 2020. A novel self-centring drill bit design for low-trauma bone drilling. *Int. J. Mach. Tools Manuf.* 154, 103568 <https://doi.org/10.1016/j.ijmactools.2020.103568>.
- Stephan, K., Laesecke, A., 1985. The thermal conductivity of fluid air. *J. Phys. Chem. Ref. Data* 14, 227–234. <https://doi.org/10.1063/1.555749>.
- Sugihara, T., Kobayashi, R., Enomoto, T., 2021. Direct observations of tribological behavior in cutting with textured cutting tools. *Int. J. Mach. Tools Manuf.* 168, 103726 <https://doi.org/10.1016/j.ijmactools.2021.103726>.
- Sugita, N., Mitsuishi, M., 2009. Specifications for machining the bovine cortical bone in relation to its microstructure. *J. Biomech.* 42, 2826–2829. <https://doi.org/10.1016/j.jbiomech.2009.08.017>.
- Sugita, N., Ishii, K., Sui, J., Terashima, M., 2014. Multi-grooved cutting tool to reduce cutting force and temperature during bone machining. *CIRP Ann. - Manuf. Technol.* 63, 101–104. <https://doi.org/10.1016/j.cirp.2014.03.069>.
- Tan, C., Zou, J., Li, S., Jamshidi, P., Abena, A., Forsey, A., Moat, R.J., Essa, K., Wang, M., Zhou, K., Attallah, M.M., 2021. Additive manufacturing of bio-inspired multi-scale hierarchically strengthened lattice structures. *Int. J. Mach. Tools Manuf.* 167, 103764 <https://doi.org/10.1016/j.ijmactools.2021.103764>.
- Wiggins, K., Malkin, S., 1978. Orthogonal machining of bone. *J. Biomech. Eng.* 100, 122. <https://doi.org/10.1115/1.3426202>.
- Yan, J., Clifton, K.B., Mecholsky, J.J., Reep, R.L., 2006. Fracture toughness of manatee rib and bovine femur using a chevron-notched beam test. *J. Biomech.* 39, 1066–1074. <https://doi.org/10.1016/j.jbiomech.2005.02.016>.
- Yang, Z.C., Zhu, L.D., Zhang, G.X., Ni, C.B., Lin, B., 2020. Review of ultrasonic vibration-assisted machining in advanced materials. *Int. J. Mach. Tools Manuf.* 156, 103594 <https://doi.org/10.1016/j.ijmactools.2020.103594>.
- Zhang, Y., Robles-Linares, J.A., Chen, L., Liao, Z., Shih, A.J., Wang, C., 2022. Advances in machining of hard tissues – from material removal mechanisms to tooling solutions. *Int. J. Mach. Tools Manuf.* 172, 103838 <https://doi.org/10.1016/j.ijmactools.2021.103838>.